Natural killer cells associate with epithelial cells in the pancreatic ductal adenocarcinoma tumor microenvironment

Zoe X. Malchiodi[1], Robert K. Suter[1], Atul Deshpande[2], Ivana Peran[1], Brent T. Harris[3,4], Anju Duttargi[3], Min-Ju Chien[1], Samika Hariharan[1], Lucia Wetherill[1], Sandra A. Jablonski[1], Won Jin Ho[2], Elana J. Fertig[2,5,6], Louis M. Weiner[1]

[1] Department of Oncology, Georgetown Lombardi Comprehensive Cancer Center, Georgetown University Medical Center, Washington, DC, USA

[2] Department of Oncology, Sidney Kimmel Comprehensive Cancer Center, Johns Hopkins School of Medicine, Baltimore, MD, USA

[3] Department of Pathology, Georgetown University Medical Center, Washington, DC, USA

[4] Department of Neurology, Georgetown University Medical Center, Washington, DC, USA

[5] Department of Applied Mathematics and Statistics, Johns Hopkins University Whiting School of Engineering, Baltimore, MD, USA

[6] Department of Biomedical Engineering, Johns Hopkins University School of Medicine, Baltimore, MD, USA

Funding

This work is supported by grants from the National Institute of Health National Cancer Institute 5T32CA009686-27 (Training Grant in Tumor Biology, Anna Tate Riegel), F31CA261125 (Z.X.M.), Achievement Reward for College Scientists (ARCS) Foundation Scholar (Z.X.M.), P30CA51008 (L.M.W).

24

25 **Abbreviations used in this paper**

26 AdjNorm (adjacent-normal); cancer-associated fibroblast (CAF); CyTOF, cytometry by time-of-
27 flight; ECM, extracellular matrix; FCSR, Flow Cytometry Shared Resourse, FFPE, formalin-
28 fixed, paraffin-embedded; FN1, fibronectin; HTSR, Histopathology & Tissue Shared Resource;
29 IC, immunocytochemistry; IF, immunofluorescence; IMC, imaging mass cytometry; LCCC,
30 Lombardi Comprehensive Cancer Center; L-R, ligand-receptor; MMP, matrix-metalloproteinase;
31 NK cell, natural killer; cell; PDAC, pancreatic ductal adenocarcinoma; PFA, paraformaldehyde;
32 ROI, region-of-interest; TMA, tissue microarray; TME, tumor microenvironment.

33

34 **Correspondence**

35 Address correspondence to Louis M. Weiner, MD, 3970 Reservoir Rd NW, Washington, DC,
36 20057, weinerl@georgetown.edu.

37

38 **Disclosures**

39 The authors have no disclosures.

40

41 **Acknowledgments**

42 We would like to thank the following from the Georgetown University Lombardi
43 Comprehensive Cancer Center's Shared Resources (SR) (partially supported by NIH/NCI
44 P30CA51008 grant): Dr. Karen Creswell, Dan Xu, and Zhinuo Jiang at the Flow Cytometry and
45 Cell Sorting SR (partially supported NIH S10OD016213 grant), Aaron Rozeboom and Bin Li at
46 the Histopathology and Tissue SR, Dr. Junfeng Ma at the Mass Spectrometry and Analytical

Pharmacology and the Biostatistics SR for support with performing metal-conjugation, IMC, and multiplex immunofluorescence, and with providing guidance on spatial analyses. We would also like to thank the Tissue Culture and Biobanking and Microscopy and Imaging Shared Resources for support on *in vitro* assays. We also thank Ahmed Elhossiny and the Pasca Di Magliano lab at the University of Michigan for providing us with the scRNAseq dataset for analyses described here. We also thank Drs. Andrew Quong and Eric Swanson at Standard BioTools Inc. for assistance with the IMC antibody panel design and its cell segmentation pipeline, and Dr. Ludmila Danilova at Johns Hopkins University for advice on computational analyses. Schematics were created with BioRender.com.

Author contributions

Z.X.M. and L.M.W. conceived the idea, designed the study, obtained funding, and wrote the manuscript. Z.X.M. conducted experiments and analyzed the data. Z.X.M., R.K.S., A.D., and W.J.H. performed or assisted with computational analyses. Z.X.M. and R.K.S. wrote R scripts and generated the computational figures. B.H. and A.D. assisted with data collection and tissue pathology of human tissue samples. L.W. and M.C. assisted in performing 2D *in vitro* invasion experiments. M.C. assisted with RT-qPCR, flow cytometry assays, and 3D *in vitro* invasion experiments. I.P. and S.H. assisted in IMC data collection. W.J.H., E.J.F., and S.A.J. assisted with experimental design.

Data transparency statement

Code used to perform IMC and scRNAseq analyses and generate the figures is available at https://github.com/Weiner-Lab/NaturalKillerCells_PDAC. Raw .mcd files for all cores of the

pancreas tissue microarray imaged by IMC and IMC-derived datasets, including histoCAT-derived single cell files, and Seurat, SingleCellExperiment, Cytomapper and distance data matrix R objects, to reproduce figures are deposited at doi: 10.5281/zenodo.10582038. The scRNAseq data was provided to us by the Pasca Di Magliano lab at the University of Michigan, which was previously published at doi: 10.1038/s43018-020-00121-4. The authors declare that all other data supporting the findings of this study are available within the paper or its supplementary information files. All other relevant data are available from the corresponding author upon request.

78 **Graphical Abstract**

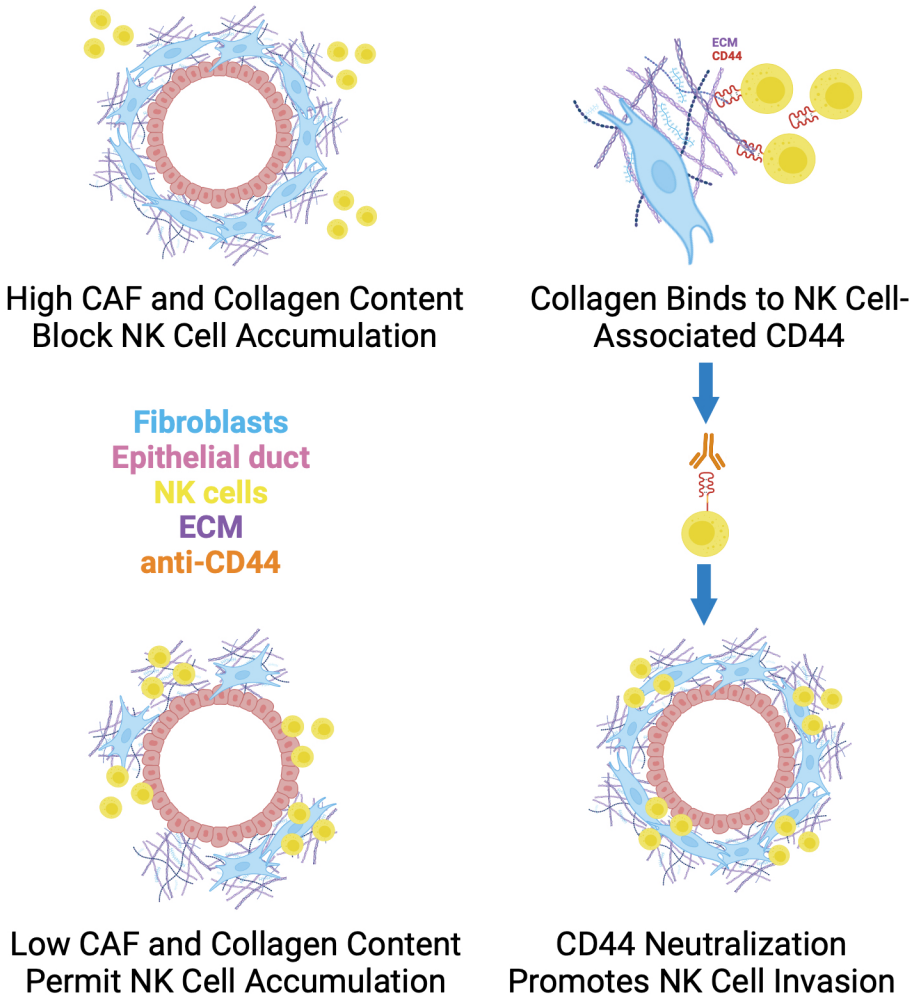

79

Abstract

Background

Pancreatic ductal adenocarcinoma (PDAC) is the most common form of pancreatic cancer. PDAC's poor prognosis and resistance to immunotherapy are attributed in part to its dense, fibrotic tumor microenvironment (TME), which is known to inhibit immune cell infiltration. We recently demonstrated that PDAC patients with higher natural killer (NK) cell content and activation have better survival rates. However, NK cell interactions in the PDAC TME have yet to be deeply studied. We show here that NK cells are present and active in the human PDAC TME.

Methods

We used imaging mass cytometry (IMC) to assess NK cell content, function, and spatial localization in human PDAC samples. Then, we used CellChat, a tool to infer ligand-receptor interactions, on a human PDAC scRNAseq dataset to further define NK cell interactions in PDAC.

Results

Spatial analyses showed for the first time that active NK cells are present in the PDAC TME, and both associate and interact with malignant epithelial cell ducts. We also found that fibroblast-rich, desmoplastic regions limit NK cell infiltration in the PDAC TME. CellChat analysis identified that the CD44 receptor on NK cells interacts with PDAC extracellular matrix (ECM) components such as collagen, fibronectin and laminin expressed by fibroblasts and malignant epithelial cells. This led us to hypothesize that these interactions play roles in regulating NK cell motility in desmoplastic PDAC TMEs. Using 2D and 3D *in vitro* assays, we found that CD44 neutralization significantly increased NK cell invasion through matrix.

Conclusions

Targeting ECM-immune cell interactions may increase NK cell invasion into the PDAC TME.

Keywords

Pancreatic ductal adenocarcinoma; natural killer cells; single cell multi-omics; tumor microenvironment.

109 **Introduction**

110 Pancreatic ductal adenocarcinoma (PDAC) is the most common form of pancreatic
111 cancer, with a 5-year survival rate of 12%.[1] PDAC is slated to become the most common
112 contributor to cancer-related deaths in coming years, thus there is a need for the identification of
113 novel therapeutic approaches.[2] PDAC is considered to be immunologically "cold" as its tumor
114 microenvironment (TME), accounting for at least 50% of the tumor volume,[3] is primarily
115 desmoplastic as a result of extracellular matrix (ECM) production by cancer-associated
116 fibroblasts (CAFs), causing resistance to therapies, poor immunogenicity and immune cell
117 infiltration.[4-7] Therefore, resolution of intratumoral cellular interactions within the PDAC TME
118 is essential to identifying novel therapeutic approaches to treat this disease.

119 In recent years, immune-stromal cell interactions have been studied in a variety of
120 diseases using emerging spatial technologies to further investigate cellular interactions that may
121 have been missed through other conventional single-cell methodologies.[8-14] However, the roles
122 and functions of natural killer (NK) cells in many solid tumors, including PDAC, remain to be
123 elucidated. NK cells are cytotoxic effector cells of the innate immune system that are known to
124 elicit anti-tumor effects.[15-18] We recently demonstrated that increased NK cell content was
125 correlated with a statistically significant increase in overall patient survival, and that NK cells are
126 necessary to elicit anti-tumor responses in a pre-clinical murine PDAC model.[15] However, NK
127 cells remain understudied in this disease.

128 Here, we used multi-omics approaches to investigate the cellular relationships of NK
129 cells within the human PDAC TME. First, we used imaging mass cytometry (IMC), a spatial
130 proteomics platform that maintains tissue architecture while capturing single cell data,[19] and
131 found that active NK cells co-localize, interact, and form a strong network with epithelial cells;

132 importantly, this co-localization was inversely related to fibroblast abundance and collagen-I
133 expression in the human PDAC TME. Secondly, we used a ligand-receptor network inference
134 tool, CellChat, to infer NK cell interactions in human PDAC scRNAseq samples and found that
135 the CD44 receptor on NK cells interacts with collagens, laminins, and fibronectin ligands on
136 malignant epithelial cells and fibroblasts; this has not been previously described. Since these
137 proteins are also present within the stroma of solid tumors, we hypothesized that neutralizing
138 CD44-mediated interactions with NK cells would increase NK cell invasion in the PDAC TME
139 and found that NK cell invasion through collagen-containing matrices significantly increased
140 upon CD44 neutralization. Hence, the human PDAC TME actively excludes invasion of NK
141 cells through the expression of ECM components, such as collagens. These results further
142 suggest a role for manipulating NK cell interactions to promote NK cell migration into the
143 PDAC TME and improve immunotherapy directed against this malignancy.

144 **Methods**

145 **Tissue samples**

146 The Lombardi Comprehensive Cancer Center (LCCC) Histopathology & Tissue Shared
147 Resource (HTSR) provided formalin-fixed, paraffin-embedded (FFPE) human PDAC and spleen
148 tissue samples. For IMC, we used a LCCC-curated FFPE human pancreas tissue microarray
149 (TMA) slide series containing 2 mm cores from normal pancreas, pancreatitis, pancreatic
150 neuroendocrine tumors, intraductal papillary mucinous neoplasm, pancreatic mucinous
151 adenocarcinoma, PDAC, colon adenocarcinoma, testicle, tonsil, and placenta samples, and
152 PDAC cell lines. Information for all TMA samples are available at doi:
153 10.5281/zenodo.10582038. This study was restricted to 44 cores from 21 previously untreated
154 PDAC patients who underwent Whipple resections or distal pancreatectomies (**Supplementary**
155 **Table S2**).

156

157 **Antibody validation, metal-conjugation, and imaging mass cytometry**

158 For IMC, we designed a metal-conjugated antibody panel. Carrier-free antibodies not
159 commercially metal-conjugated were validated by immunofluorescence (IF) in PDAC or spleen
160 tissue (**Supplementary Table S1**). Antibodies with expected expression patterns were metal-
161 conjugated using MaxPar X8 Multimetal Labeling Kits (Standard Bio Tools (SBI);
162 **Supplementary Table S1**). Metal-conjugation was validated by cytometry by time-of-flight
163 (CyTOF) (Hyperion Imaging System; SBI) at the LCCC Flow Cytometry Shared Resource
164 (FCSR). Metal-conjugated antibody dilutions were optimized in the pancreas TMA prior to final
165 IMC staining at the HTSR. Antigen retrieval and staining was performed (SBI) at the LCCC
166 HTSR, while image acquisition was performed at the LCCC Mass Spectrometry and Analytical

167 Pharmacology Shared Resource. A maximum of 2.25 mm^2 regions of interest (ROIs) on TMA
168 cores were selected, laser-ablated and analyzed by CyTOF to quantitate the metal-conjugated
169 antibodies per ROI, generating multiplex images.[20, 21] All data were collected using the Hyperion
170 Imaging System (SBI) and qualitatively validated in MCD Viewer (v1.0.560.6; SBI) and QuPath
171 softwares.
172
173 **IMC image processing, data transformation, and single-cell clustering**
174 Raw IMC data was processed following the widely used ImcSegmentationPipeline
175 (https://github.com/BodenmillerGroup/ImcSegmentationPipeline).[11, 22-24] In the Ilastik software,
176 DNA, E-cadherin, pan-cytokeratin, vimentin, and CD45RO markers were used to pixel-train and
177 generate cell segmentation probability maps for nuclear, cytoplasmic, cell membrane, and
178 background areas in all IMC images, which were imported into CellProfiler to generate cell
179 segmentation masks to then extract single cell data using histoCAT.[25, 26] 412,862 cells were
180 identified across 44 images from 21 PDAC patient samples. Extracted IMC-derived single cell
181 data were imported into R (v4.2.1) for downstream computational analyses. histoCAT-derived
182 single cell data files generated are available at doi: 10.5281/zenodo.10582038. All scripts
183 adapted from this pipeline for downstream analyses are available at https://github.com/Weiner-
184 Lab/NaturalKillerCells_PDAC. Single cell protein expression data was log-transformed, re-
185 integrated, and clustered using Seurat-based analysis.[27] Using a supervised clustering with
186 canonical cell markers (αSMA, CD3, CD4, CD8α, CD11b, CD16, CD20, CD45RO, CD56,
187 CD68, E-cadherin, FAP, FOXP3, NKG2D, NKp44, pan-cytokeratin, vimentin), we found that a
188 clustering resolution = 0.35 provided distinct immune, fibroblast, and epithelial cell populations.
189 Each cell population was subsetted and re-clustered to identify the functional state of subclusters

190 using the following markers: CD69, CD107α, cleaved-caspase 3, collagen-I, granzyme B, HLA-
191 A/B/C, HLA-A1, IFNγ, Ki67, MICA, PCNA, perforin, PD-1, PD-L1, and TGFβ. All subclusters
192 were reintegrated, annotated, and 29 unique cell populations were identified and validated
193 visually using the Cytomapper R package and MCD Viewer. Seurat objects containing all the
194 PDAC single cell metadata is available at doi: 10.5281/zenodo.10582038 and were converted to
195 SingleCellExperiment[28] objects for downstream spatial analyses.
196

197 **IMC spatial analysis**

198 We generated knn-based interaction graphs for the 15-nearest neighbors and used k-
199 means clustering to group cells into 8 distinct cellular neighborhoods using the
200 SpatialExperiment and imcRtools R packages.[24, 29-31] Using the imcRtools package, permutation
201 test-based cell-cell interaction analysis identified significant interactions or avoidances between
202 cell populations. Using FDR analysis, cell-cell interactions with $P < 0.01$ were considered
203 significant. Based on Euclidean distance metadata, distance and network analyses were
204 performed, as previously described.[9] Seurat's CellSelector function[27] was used to select and
205 quantify cells in epithelial-ductal ROIs of spatial images. From CellSelector, percentages of cell
206 populations in each epithelial-ductal ROI were quantified, and epithelial-ductal ROIs were
207 stratified in quartiles based on fibroblast abundance (Q1 = low fibroblast quartile, Q4 = high
208 fibroblast quartile). Mean total expression of all markers was quantified in representative
209 epithelial-ductal ROIs of pseudoimages using MCD Viewer. Cell-based expression in epithelial-
210 ductal ROIs was performed using Seurat.
211

212 **Immunofluorescence**

213 Human PDAC samples were used for multiplex IF to assess pan-cytokeratin, E-cadherin,
214 CD56, and NKG2D (**Supplementary Table S3**). Patient samples were from 4 males and 2
215 females with age ranges between 44-86, and had tumor diameters ranging from 3.7-18 cm.
216 Multiplex staining and imaging were performed as previously described,[32] except tissue images
217 were captured using Akoya Biosciences Inc.'s PhenoImager Fusion imaging platform at the
218 LCCC HTSR. Images were exported as *.qtiff* files and visualized using QuPath software.
219

220 **Single-cell RNA-sequencing analysis**

221 To infer ligand-receptor (L-R) interactions in PDAC, we utilized a previously published
222 human PDAC scRNAseq dataset[33] and subsetted NK cells, fibroblasts, and epithelial cells.
223 Malignant and normal epithelial cells were differentiated using CytoTRACE, a computational
224 framework that predicts cellular differentiation states by measuring the number of genes
225 expressed by each cell.[34] The CytoTRACE scores distribution was observed to be bi-modal and
226 using a mixed-model, an ideal cut-off value separating the two distributions was determined to
227 be 0.72 where scores greater than 0.72 indicated a malignant epithelial cells (**Supplementary**
228 **Figure S7**).[35] We then used CellChat, a manually curated protein database of approximately
229 2,000 L-R pairs[36] to infer potential L-R interactions between these cell populations. A wilcox test
230 with a Bonferroni correction from the FindMarkers Seurat function (v4.3) was used for
231 differential gene expression analysis of CellChat-identified L-R genes. Genes with an adjusted P
232 < 0.01 were considered significantly differentially expressed. R scripts for applied CytoTRACE
233 and CellChat analyses are available at https://github.com/Weiner-Lab/NaturalKillerCells_PDAC.
234

235 **Cell culture**

236 Human PANC-1 PDAC cells and donor NK cell lines were cultured, as previously
237 described,[37] except donor NK cells received 0.5% v/v of IL-2. Donor NK cells were stimulated
238 with the engineered K562 cell line, K562-mb21-41BBL (courtesy of Dr. Dean Lee at
239 Nationwide Children's).[38] K562-mb21-41BBL cells were cultured in supplemented RPMI (10%
240 FBS, 1% penicillin/streptomycin). For NK cell stimulation, K562-mb21-41BBL cells were
241 collected (5 minutes, 1,000 rpm, 4˚C), resuspended in supplemented RPMI with mitomycin C
242 (Sigma-Aldrich) (C_f = 0.01 mg/ml) and incubated for 4 hours (37˚C). Pre-treated K562-mb21-
243 41BBL cells were collected (5 minutes, 1,000 rpm, 4˚C), resuspended in NK cell medium, then
244 co-cultured with donor NK cells (E:T = 1:1); this process was repeated at least once per week.
245 Donor NK cells aged day 1-50 and stimulated 1-3 days prior to *in vitro* assays were used.
246
247 **Flow cytometry**
248 Cells were centrifuged (5 minutes, 1,000rpm, 4˚C) washed twice (1X PBS), then
249 resuspended in FACS staining buffer (1% BSA in 1X PBS). Human Fc block (BD Pharmigen,
250 CAT#: 564219) then α-CD44-BV605 (Biolegend, CAT#: 103047) antibodies were added per
251 manufacturer's recommendations (30 minutes, 4˚C). Cell pellets were washed twice (FACS
252 staining buffer), resuspended in fixative (1% PFA in 1X PBS), then processed by the LCCC
253 FCSR in a BD LSRFortessa Cell Analyzer (BD Biosciences). Analysis was performed using
254 FlowJo (v10.8.1).
255
256 **NK cell 2D invasion assay**
257 The bottom of 5 µm Transwells (Corning) were coated with Matrigel (Corning) diluted
258 1:3 in NK cell medium. CXCL9 (C_f =100 ng/ml) (R&D Systems)-supplemented NK cell

259 medium was added to the bottom of each well. Donor NK cells were added to Transwells with or
260 without an α-CD44 neutralizing antibody (clone IM7; Bio X Cell; C_f = 10 µg/ml) and incubated
261 for 4 hours (37˚C). Transwells were removed, cells were stained with Trypan Blue Stain (Gibco)
262 and manually counted on a hemocytometer. Control cells were plated without Transwells to
263 count total cells to calculate percent invasion. Relative invasion is the percent of cells that
264 invaded through the transwell normalized to untreated NK cell conditions. A Wilcoxon matched-
265 pairs signed rank test was performed to determine statistical significance (GraphPad Prism v10).
266

267 **NK cell 3D spheroid invasion assay**

268 As previously described,[39, 40] PANC-1 cells were seeded in each well of a low-adhesion
269 U-bottom plate, spun (5 minutes, 1,000 rpm, 4˚C) and cultured overnight. Spheroids were
270 embedded with donor NK cells in an 80:20 Collagen-I (Invitrogen): Matrigel (Corning) mixture
271 in chamber wells (Lab-Tek). Embedded spheroids were treated with α-CD44 (clone IM7; Bio X
272 Cell; C_f = 10 µg/ml) for 24 hours (37˚C) prior to immunocytochemistry (IC). For IC, samples
273 were fixed with 4% paraformaldehyde (PFA; 10 minutes, 25˚C), washed for with 1X PBS (5
274 minutes), then permeabilized with 0.5% Triton-X100 (10 minutes). Cells were washed once,
275 blocked (1% BSA in 1X PBS, 30 minutes), then incubated with human Fc block (BD Pharmigen,
276 CAT#: 564219). Samples were incubated with α-pan-cytokeratin- eFluor™ 660 (Invitrogen,
277 CAT#: 50-9003-82) and α-CD56 (Invitrogen, CAT#: MA1-19129) antibodies overnight (25˚C).
278 An α-Mouse IgG2a-AF488 secondary antibody (Invitrogen, CAT#: A-21131; 1-4 hours, 25˚C),
279 cells were washed 3 times, incubated with DAPI (50 ng/ml; 10 minutes, 25˚C), then washed
280 twice. Coverslips were mounted with anti-fade mountant, then and dried. Z-stacks of spheroids
281 were imaged using a Leica SP8 AOBS microscope at the LCCC Microscopy and Imaging Shared

282 Resource. Z-stacks were ≤ 1 µm. Z-stack images were processed and using FIJI software
283 (v2.14.0) for manual NK cell quantitation into PANC-1 spheroids. Statistical significance was
284 determined using a Wilcoxon matched-pairs signed rank test (GraphPad Prism v10).
285

286 **Effects of CD44 neutralization on MMP gene expression in human NK cells**

287 Donor NK cell lines were incubated with or without α-CD44 (clone IM7; Bio X Cell; C_f
288 = 10 µg/ml) for 1 and 4 hours. Cells were collected (5 minutes, 1,000 rpm, 4˚C) and RNA was
289 isolated using the PureLink™ RNA Mini Kit (Ambion). RNA concentration was measured using
290 NanoDrop 8000 (ThermoFisher Scientific), then stored at -80˚C. Diluted RNA (20 ng/µl) was
291 treated with 10% v/v 10X DNase I Buffer and 10% v/v DNase I (Promega; 15 minutes, 25˚C).
292 10% v/v of RQ1 RNase/DNase Stop Solution (Promega) and 10% v/v Oligo(dT) nucleotides
293 (IDT) were added, then heat inactivated at 65˚C (10 minutes) then at 4˚C (5 minutes). cDNA was
294 synthesized with the GoScript™ Reverse Transcriptase Kit (Promega). qPCR was performed
295 using GoTaq qPCR Master Mix (Promega) with the StepOnePlus™ Real-Time PCR System
296 (ThermoFisher Scientific). Gene expression was quantified ($2^{-\Delta C_T}$; Ambion) using *HPRT*
297 (Forward 3'→5': CTTTCCTTGGTCAGGCAGTA, reverse 3'→5':
298 TGGCTTATATCCAACACTTCG) as an internal, endogenous control. Fold-change was
299 calculated using the $2^{-\Delta\Delta C_T}$ method and a One-Way ANOVA, Kruskal-Wallis test was performed
300 to determine statistical significance (GraphPad Prism v10).
301

302 **Ethics statement**

303 The human pancreas TMA used in this study was approved by the Georgetown University LCCC
304 Biospecimen Use Committee.

305 **Results**

306 **Spatial proteomic analysis of the human PDAC TME resolves PDAC cell populations**

307 To resolve the spatial landscape of the human PDAC TME, we performed IMC, a spatial
308 proteomics platform that maintains tissue architecture while capturing single cell data by using
309 metal-conjugated antibodies, eliminating autofluorescence from typical fluorescence-based
310 imaging, allowing for an increase in size of antibody panels to up to 40 markers. Using CyTOF
311 technology, tissue images are reconstructed with single cell resolution to enable higher order single
312 cell proteomic and spatial analyses.[19, 41, 42] For IMC, we designed a metal-conjugated antibody
313 panel containing epithelial cell, immune cell, and fibroblast markers (**Supplementary Table S1**)
314 and probed a human pancreas tissue microarray (TMA) curated at the Lombardi Comprehensive
315 Cancer Center (LCCC) Histopathology & Tissue Shared Resource (HTSR) containing primary
316 tumor samples from 21 untreated PDAC patients (**Supplementary Table S2**). Following a known
317 IMC cell segmentation pipeline[23-26] (**Figure 1A**), we identified 412,862 cells in 44 IMC
318 pseudoimages from these patients. Single-cell protein expression data were extracted using
319 histoCAT[26] for downstream single-cell proteomic and spatial analyses in R. Using Seurat-based
320 analysis, expression data was log-normalized and cell populations were identified using supervised
321 clustering approaches.[43] Canonical cell phenotype markers (CD11b, CD16, CD20, CD3,
322 CD45RO, CD4, CD56, CD68, CD8α, E-cadherin, FAP, FOXP3, NKG2D, NKp44, αSMA, pan-
323 cytokeratin, vimentin) were used to distinguish between immune cells, epithelial cells, and
324 fibroblasts during cell clustering, which identified 8 predominant cell types (**Figure 1B-C**):
325 αSMA^+ fibroblasts, B cells, $CD4^+$ T cells, $CD8^+$ T cells, epithelial cells, FAP^+ fibroblasts,
326 macrophages, and NK cells. These main cell types were then subclustered to identify the functional
327 state of these cell populations using the remaining markers in our IMC panel (**Supplementary**

Table S1), and we identified 29 distinct clusters to define active, proliferative, and apoptotic cell states (**Supplementary Figure S1**). As expected in PDAC, the majority of cells were fibroblasts and epithelial cells, and we were able to define distinct immune cell populations, including NK cells (**Figure 1E-F**). We also observed that within our patient samples that there was a similar proportion of NK cells to that of $CD4^+$ and $CD8^+$ T cell populations, suggesting the potential relevance of NK cells in the human PDAC TME (**Figure 1D**).

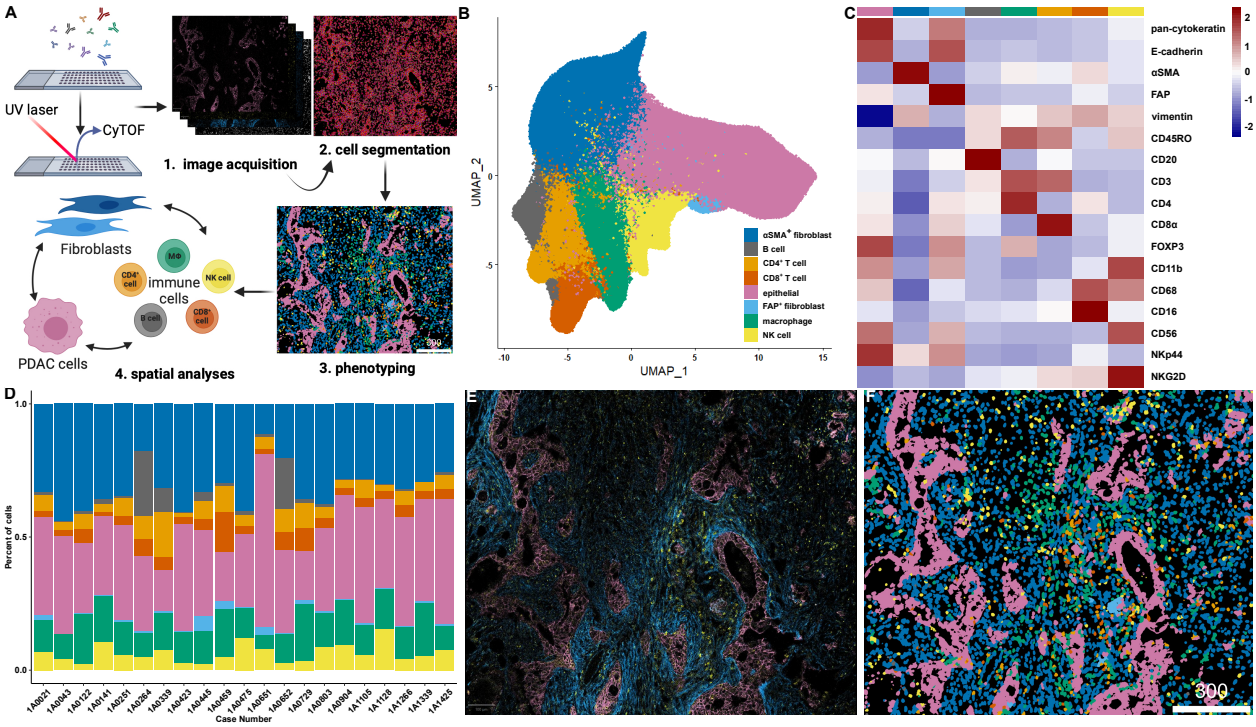

Figure 1: Spatial proteomic analysis of the human PDAC TME resolves PDAC cell populations. A. Schematic of IMC workflow. **B.** UMAP of IMC-defined cell populations from 21 untreated PDAC patient samples. **C.** Heatmap of averaged, log-normalized protein expression of canonical markers used to phenotype human PDAC cell populations (legend in **B**). **D.** Bar plot of cell percentages of cell populations per PDAC patient (legend in **B**). **E.** Representative IMC pseudoimage of the human PDAC TME highlighting distinctions between epithelial cells (pan-cytokeratin and E-cadherin; pink), fibroblasts (αSMA and FAP; blue), and immune cells

342 (CD45RO; yellow). **F.** Cytomapper image of **E** displaying all identified cell types from **B-D**,
343 colored according to the legend in **B**.
344
345 **NK cells and epithelial cells co-localize and interact in the human PDAC TME**
346 Qualitative evaluation of the IMC images suggested that NK cells co-localized with
347 epithelial cells in the human PDAC TME (**Figure 2A**). We validated NK cell-epithelial cell co-
348 localization in additional human PDAC tissue samples using multiplex immunofluorescence
349 (**Figure 2B**). To assess NK cells spatially in multicellular structures within the architecture of the
350 human PDAC TME, we performed a cellular neighborhood analysis (**Figure 2C**).[31] Briefly, this
351 neighborhood analysis aims to define characteristic groups of cellular co-localization from
352 spatial proteomics atlas datasets. Using this technique, we defined 8 distinct cellular
353 neighborhoods where cellular neighborhoods 1, 2, and 6 formed distinct structures representative
354 of epithelial-ductal regions, and both cellular neighborhoods 2 and 6 of epithelial-ductal regions
355 created a distinct tumor-stroma border (**Supplementary Figure S2**). Interestingly, we found that
356 cellular neighborhood 2 had a high composition of epithelial and NK cell populations (**Figure**
357 **2C**), and NK cells were more abundant than $CD4^+$ and $CD8^+$ T cells within the epithelial-ductal
358 cellular neighborhoods (**Supplementary Figure S3**). We also observed that while there was
359 minimal localization of cells from cellular neighborhood 6 at the tumor-stroma border, there
360 appeared to be a greater abundance of cells from cellular neighborhood 4, which was immune-
361 rich. Conversely, in epithelial-ductal regions encased with cells from cellular neighborhood 6,
362 primarily composed of proliferative epithelial cells and proliferative FAP^+ fibroblast populations,
363 there appeared to be more cells from cellular neighborhood 5, which was αSMA^+ fibroblast-rich
364 (**Supplementary Figures S2-S3**). These observations suggest that fibroblast-rich regions support

365 epithelial cell proliferation and prevent immune cell infiltration, supporting the concept that
366 fibroblasts act as immune decoys or deterrents in the PDAC TME.

367 While the majority of immune cells exist in cellular neighborhood 4, which also contains
368 the highest abundance of apoptotic epithelial cells, we observed that cellular neighborhood 8 had
369 the second highest abundance of apoptotic epithelial cells and active NK cells (**Figure 2C**),
370 suggesting that NK cells in these regions mediated anti-tumor immune responses. Of note, the
371 proportion of NK cells in cellular neighborhood 8 was larger than that of other immune cell
372 populations (**Supplementary Figures S3**). We also observed that cellular neighborhood 2
373 contained the highest abundance of IFNγ^+ epithelial cells; interestingly, NK cells comprised the
374 largest immune cell population in cellular neighborhood 2 (**Figure 2C**). These observations
375 support the hypothesis that NK cells are cytotoxic to malignant epithelial cells in human PDAC
376 and demonstrate that spatial analysis identifies NK cell-epithelial cell co-localization.

377 To further characterize significant cell-cell pairwise interactions, we performed a cellular
378 interaction analysis, a permutation test of these pairwise interactions,[26] to reveal cell populations
379 with significant interactions or avoidances. The cellular interaction analysis demonstrated that
380 NK cell populations interact with apoptotic epithelial cells more strongly than other active
381 immune cell subsets (**Figure 2D**), including active CD8$^+$ T cells. This phenomenon has not been
382 previously described and suggests that NK cells play an important role in anti-tumor immune
383 responses in the PDAC TME.

384 Next, we performed Euclidean distance-based analysis[9, 44] to quantitate NK cell
385 proximity to other cells in the PDAC TME, revealing that epithelial cells were in close proximity
386 to NK cells (**Figure 2E**). Interestingly, αSMA$^+$ fibroblasts were the closest fibroblast population
387 to NK cells, suggesting that NK cells that do not form strong interrelationships with epithelial

388 cells may be engaged and inhibited by stromal elements. To further contextualize the cellular
389 communication network in the PDAC TME, we performed a cellular network analysis, using
390 previously described methods,[9] where each node represents a distinct cell population (**Figure 2F**,
391 **Supplementary Figure S1**). In this network graph (**Figure 2F**), NK cell nodes were surrounded
392 by epithelial cell nodes and distant from $CD4^+$ and $CD8^+$ T cell nodes. Of note, the apoptotic
393 epithelial cell node was surrounded by NK cell and macrophage nodes and did not form strong
394 relationships with T cell nodes. These findings further demonstrate the relevance of innate
395 effectors cells in the human PDAC TME.

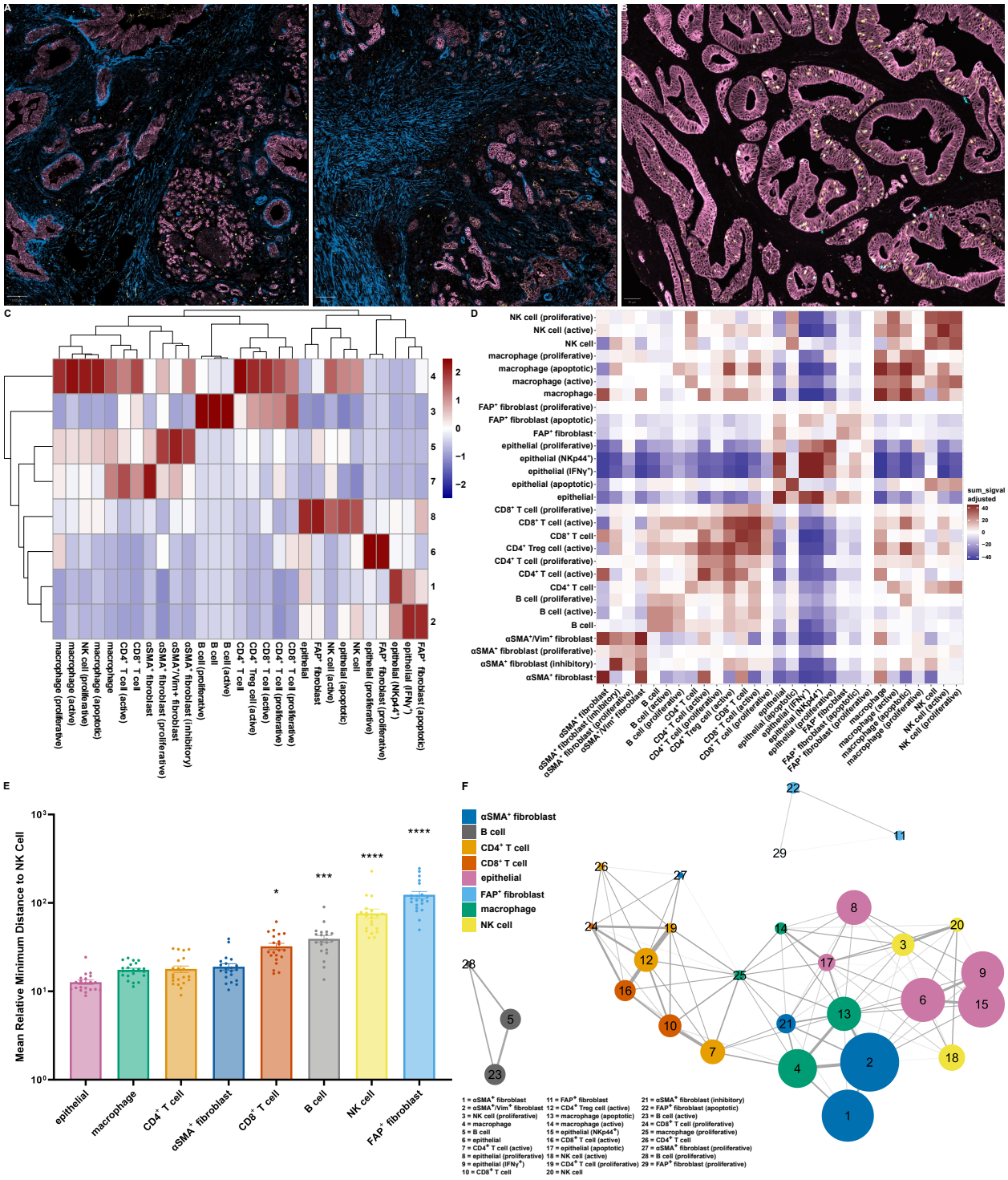

Figure 2: NK cells co-localize and interact with epithelial cells in the human PDAC TME. **A.** Representative IMC pseudoimages displaying NK cell-epithelial cell co-localization (αSMA = blue; E-cadherin, pan-cytokeratin = pink; NKG2D = yellow, scale bar = 100 µm). **B.**

400 Representative multiplex immunofluorescence image of human PDAC showing NK cell-
401 epithelial cell co-localization (n = 6; pan-cytokeratin = pink, CD56 = yellow, NKG2D = cyan,
402 scale bar = 50 μm). **C.** Cellular neighborhood analysis revealed 8 distinct cellular neighborhoods
403 (red = high proportion of cells within cellular neighborhoods, blue = low proportion of cells
404 within cellular neighborhoods). **D.** Cellular interaction analysis (blue = strong avoidance, red =
405 strong interaction; FDR, $P < 0.01$) of IMC-defined cell subpopulations. **E.** Distance analysis per
406 patient (n = 21) revealed that epithelial cells in PDAC are the closest to NK cells. Cell
407 populations that were significantly distant from epithelial cells were calculated using 2-way
408 ANOVA, Kruskal-Wallis test (*$P < 0.05$, ***$P < 0.001$, ****$P < 0.0001$;). **F.** Network graph of
409 the top 75% of interactions between all IMC-defined cell populations in human PDAC showing
410 epithelial cells and NK cells exist in similar networks.
411
412 **NK cell abundance in human PDAC epithelial-ductal ROIs inversely relates to both**
413 **fibroblast abundance and Collagen-I expression**
414 While we observed significant NK cell-epithelial cell spatial relationships in the human
415 PDAC TME, as demonstrated by cellular neighborhood, cellular interaction, distance, and
416 network analyses (**Figure 2**), a hallmark phenotype of PDAC is the high abundance of CAFs that
417 are known to cause immune suppression and decrease immune cell infiltration.[6] Therefore, we
418 hypothesized that epithelial-ductal ROIs with high fibroblast abundance would have a decrease
419 in immune cell infiltration. To test this hypothesis, we identified ROIs from epithelial-ductal
420 structures previously defined by cellular neighborhood analysis (**Figure 2**, **Supplementary**
421 **Figure S2**). We then used the CellSelector function from Seurat[27] to isolate these ROIs on IMC-
422 derived single-cell spatial images for downstream analysis to quantify the abundance of each cell

423 population within these epithelial-ductal ROIs. The abundance of cell populations was quantified
424 as the percentage of the total cells within each epithelial-ductal ROI. After quantification,
425 epithelial-ductal ROIs were stratified into quartiles based on their percentage of fibroblast
426 abundance (**Figure 3**). We first confirmed statistically significant increases in fibroblast
427 abundance across the fibroblast abundance quartiles we defined (**Figure 3A**). We also found
428 statistically significant decreases in both NK cell and epithelial cell abundance across fibroblast
429 abundance quartiles (**Figure 3B-C**). Conversely, proliferative epithelial cells significantly
430 increased across fibroblast abundance quartiles (**Supplementary Figure S4E**), supporting
431 observations from cellular neighborhood analysis (**Figure 2C**, **Supplementary Figure S2**).
432 Interestingly, NKp44^{+} and IFNγ^{+} epithelial cell populations significantly decreased across
433 fibroblast abundance quartiles (**Supplementary Figure S4E**). As cellular neighborhood analysis
434 identified NK cells to be the most abundant cell population in cellular neighborhoods with
435 NKp44^{+} and IFNγ^{+} epithelial cell populations (**Figure 2C**, **Supplementary Figure S2-3**), this
436 suggests that NK cell functionality may be decreasing in epithelial-ductal ROIs with high
437 fibroblast abundance. Of note, there was no statistically significant difference in CD8^{+} T cell
438 abundance across fibroblast abundance quartiles (**Supplementary Figure S6**), supporting
439 previous observations of T cell localization in desmoplastic regions in PDAC.[45]
440 To determine if decreased NK cell infiltration across fibroblast abundance quartiles
441 correlated with cell functionality, we quantified the total expression of functional markers
442 (CD69, CD107α, cleaved-caspase 3, collagen-I, granzyme B, HLA-A/B/C, HLA-A1, IFNγ,
443 Ki67, MICA, PCNA, perforin, PD-1, PD-L1, TGFβ), from the IMC antibody panel
444 (**Supplementary Table S1**), within these epithelial-ductal ROIs and observed no significant
445 difference in the total expression of the immune cell activation markers (CD69, CD107α,

446 granzyme B, perforin) within the PDAC TME (**Supplementary Figure S6**). We further
447 evaluated the cellular-based expression of these functional markers in NK cell populations within
448 these epithelial-ductal ROIs and observed that NK cells were more active in epithelial-ductal
449 ROIs with low fibroblast abundance as they exhibited higher expression of known immune cell
450 activation markers, including CD69, CD107α, granzyme B, and IFNγ (**Figure 3G-K**). While
451 there were no significant differences in the abundance of apoptotic epithelial cells across
452 fibroblast abundance quartiles of epithelial-ductal ROIs (**Supplementary Figure S4**), we did
453 observe that epithelial cells expressed more cleaved-caspase 3, an apoptosis marker, in epithelial-
454 ductal ROIs of lower fibroblast abundance (**Figure 3L**). These data demonstrate that NK cell
455 cytotoxic function is retained in epithelial-ductal ROIs with lower fibroblast abundance where
456 NK cells are more co-localized with epithelial cells. Since fibroblasts are known to deposit
457 collagen within the stroma, we measured the intensity of collagen-I expression within these
458 epithelial-ductal ROIs and found a statistically significant increase in total collagen-I expression
459 across fibroblast abundance quartiles (**Figure 3D**). These findings suggest that fibroblasts protect
460 and enhance the growth of malignant epithelial cells in the PDAC TME, in agreement with
461 known fibroblast biology, and also suggest that NK cell cytolytic function and infiltration into
462 malignant epithelial-ductal ROIs is inhibited by desmoplasia.

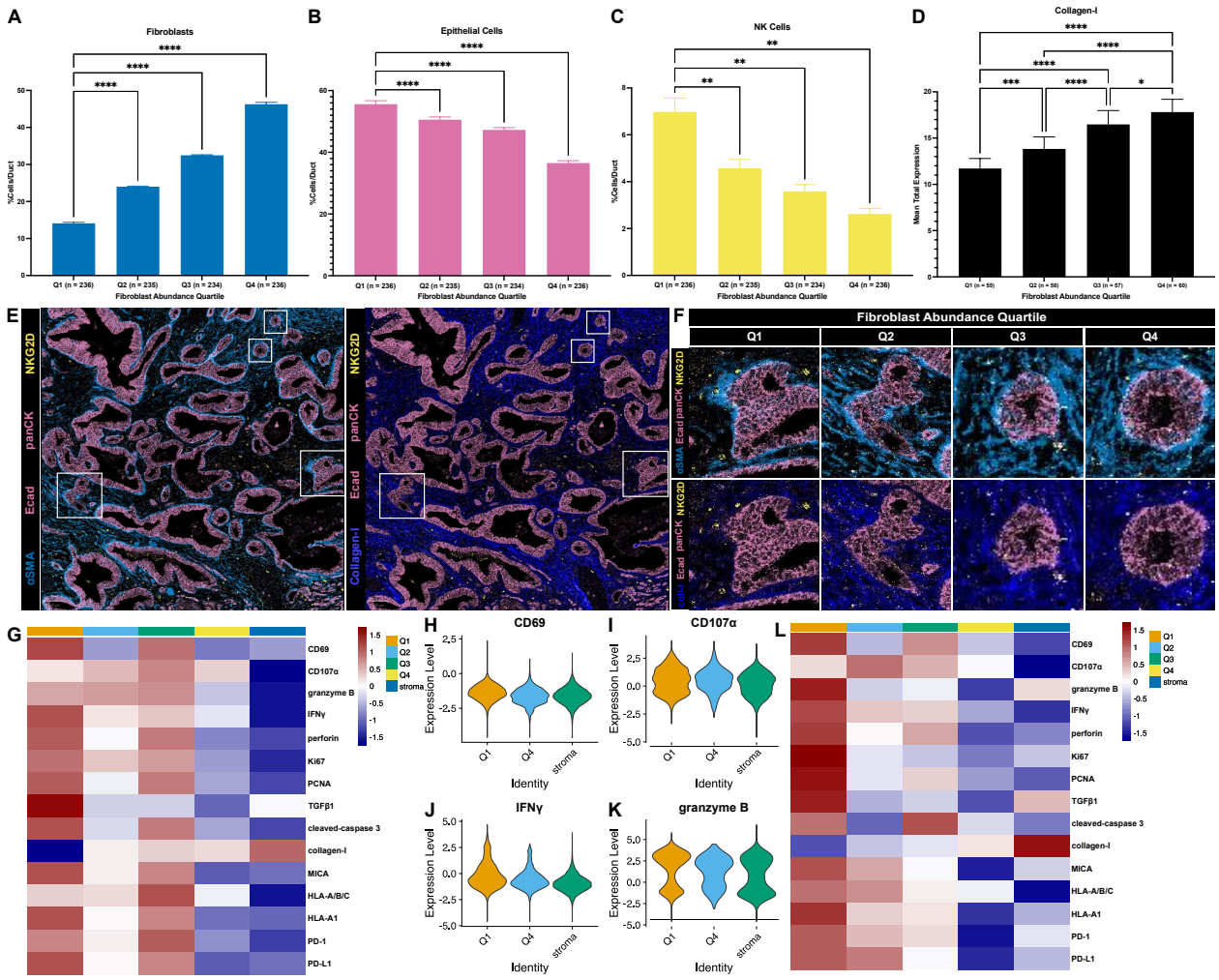

Figure 3: NK cell abundance in human PDAC epithelial-ductal ROIs inversely relates to both fibroblast abundance and Collagen-I expression. Quantitation of **A.** total fibroblasts, **B.** epithelial cells, and **C.** NK cells in epithelial-ductal ROIs ranked by fibroblast abundance quartile (2-way ANOVA; ****$P < 0.0001$; n = 952, total epithelial-ductal ROIs). **B.** Quantitation of total collagen-I expression in epithelial-ductal ROIs ranked by fibroblast abundance quartile (2-way ANOVA; *$P < 0.05$, ***$P < 0.001$, ****$P < 0.0001$; n = 230, total epithelial ductal ROIs). **E.** Representative IMC pseudoimages showing αSMA (left, light blue) or collagen-I (right, dark blue) with pan-cytokeratin (panCK, pink), E-cadherin (Ecad, pink), and NKG2D (yellow); scale bar = 100 µm with white boxes of each fibroblast abundance quartile. **F.** Insets of

473 representative epithelial-ductal ROIs from each fibroblast abundance quartile (Q1-Q4) shown in
474 the white insets in **E**. **G.** Heatmap of averaged, log-normalized protein expression of functional
475 markers in NK cells stratified by fibroblast abundance quartile (Q1-Q4) and stromal
476 compartments. Violin plots showing NK cell-based expression of **H.** CD69 **I.** CD107α **J.**
477 granzyme B, and **K.** IFNγ. **L.** Heatmap of averaged, log-normalized protein expression of
478 functional markers in epithelial cells stratified by fibroblast abundance quartile (Q1-Q4) and
479 stromal compartments.
480

481 **CellChat identifies CD44 as a potential mediator of interactions between NK cells with**
482 **CAFs and malignant epithelial cells in human PDAC**

483 Based on findings, from IMC analysis of the PDAC TME, that NK cells interact with
484 epithelial cells, and their infiltration is inhibited by fibroblasts, we next further elucidated their
485 potential molecular interactions using CellChat to infer ligand-receptor (L-R) interactions among
486 NK cells, fibroblasts, and epithelial cells. CellChat is a tool with a manually curated database to
487 infer L-R interactions from scRNAseq data.[36] We used this analysis pipeline against a recently
488 published human PDAC scRNAseq dataset containing adjacent-normal (AdjNorm) and PDAC
489 patient samples [33]. As malignant cells are more de-differentiated than normal, differentiated
490 cells,[46] and to infer if potential L-R pairs were from normal versus malignant epithelium, we first
491 distinguished between these two cell epithelial cell states using CytoTRACE (**Supplementary**
492 **Figure S7**), a computational framework that predicts cellular differentiation states from
493 scRNAseq data.[34]

494 Using CellChat, we assessed the interaction strength of NK cells, fibroblasts, and both
495 normal and malignant epithelial cells to determine which of these populations exhibited

496 significant changes in their outgoing or incoming signaling between AdjNorm and PDAC
497 disease states. CellChat revealed that fibroblasts demonstrate a substantial increase in outgoing
498 interaction strength in PDAC compared to fibroblasts in AdjNorm, while both NK cells and
499 malignant epithelial cells become strong receivers of cellular signals in PDAC (**Figure 4A**).
500 Normal epithelial cell signaling remains relatively unchanged between the two disease states
501 (**Figure 4A**). This suggests that fibroblasts orchestrate interactions amongst these three cell
502 populations in PDAC.

503 Accordingly, we identified the signaling pathways targeting NK cells with significant
504 changes in their communication probabilities, or activation. The collagen, fibronectin (FN1), and
505 laminin pathways became highly active, as they had the highest PDAC-enriched or PDAC-
506 specific communication probabilities based on their increased information flow (**Figure 4B**).
507 CellChat also identified ligands from these pathways to be the most highly enriched in PDAC
508 (**Supplementary Table S4**). We then investigated the L-R interactions from these pathways that
509 targeted NK cells. Using fibroblasts and epithelial cell populations as source cells and NK cells
510 as their targets, we determined that NK cells were primarily targeted by a variety of collagens,
511 laminins, and *FN1* through *CD44* on NK cells (**Figure 4C**). We next explored which of these L-
512 R pair genes were differentially expressed across disease states in these cell populations and
513 found that several genes in these L-R pairs were significantly increased in fibroblasts and
514 epithelial cell populations in PDAC samples (**Supplementary Figure S8**). Of note, while
515 malignant epithelial cells exhibited a significant increase in *CD44* gene expression, there was no
516 significant difference in normal epithelial cells nor fibroblasts (**Figure 4D-F**). Concurrently, the
517 only gene among the identified L-R pairs with a differential increase in NK cells in PDAC was
518 *CD44* (**Figure 4G**). As fibroblasts and malignant epithelial cells highly expressed collagen,

laminin, and *FN1* genes, and their protein counterparts are typically highly expressed in the TME of PDAC, it led us to hypothesize that NK cells get trapped in stromal-rich regions in the PDAC TME and that CD44 may be targetable to enhance NK cell motility to target PDAC cells.

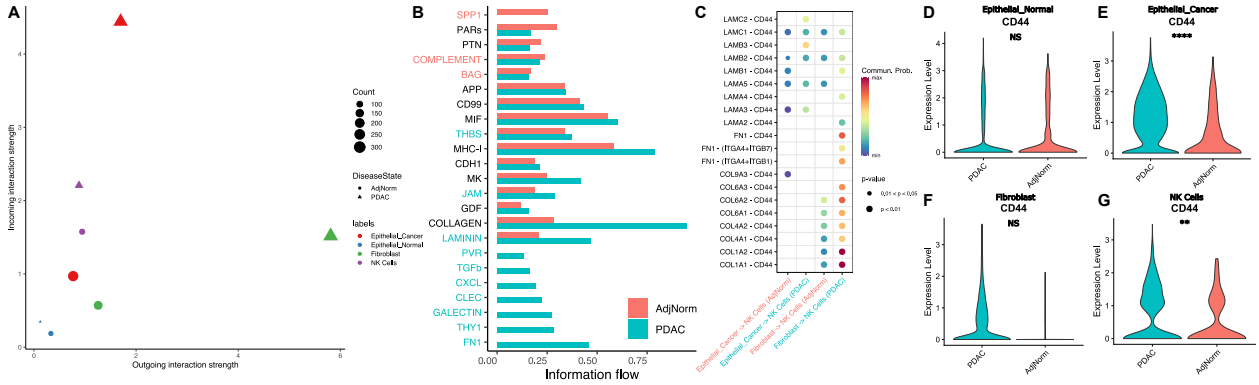

Figure 4: CellChat identifies CD44 as a potential mediator of interactions between NK cells with CAFs and malignant epithelial cells in human PDAC. A. Incoming and outgoing interaction strength for each cell population grouped by AdjNorm and PDAC disease states. **B.** Communication probabilities of signaling pathways targeting NK cells between AdjNorm and PDAC disease states as measured by information flow (pathway legend: pink = AdjNorm-specific, teal = PDAC-specific, black = equally specific). **C.** Significant ligand-receptor pairs from collagen, FN1, and laminin signaling pathways targeting NK cells upregulated in PDAC compared to AdjNorm. Violin plots showing differential expression of *CD44* between PDAC (teal) and AdjNorm (pink) disease states in **D.** normal epithelial cells, **E.** malignant epithelial cells, **F.** fibroblasts, and **G.** NK cells (NS = not significant, $^{**}P < 0.01$, $^{****}P < 0.0001$, Bonferroni correction).

CD44 neutralization increases human donor NK cell invasion *in vitro*

The CD44 glycoprotein is highly expressed by a variety of cell types. While its main ligand is hyaluronic acid (HA), which can be highly expressed by cancer and stromal cells,[47, 48]

538 CD44 is also known to bind to collagens, laminins, and FN1.[49] CD44 signaling is also known to
539 affect cellular proliferation, adhesion and migration.[48] Therefore, based on findings from
540 CellChat, we hypothesized that stromal elements in PDAC bind to CD44 on NK cells to prevent
541 NK cell invasion through the stroma to target PDAC epithelial cells. First, we validated CD44
542 expression of human donor NK cells by flow cytometry (**Supplementary Figure S9**). Since
543 collagens, laminins, and FN1 can also be found in the stroma, we assessed NK cell invasion
544 through basement-membrane and collagen-containing matrices *in vitro.* We performed a 2D
545 Boyden-Chamber Transwell assay with four human donor NK cells lines by coating the
546 Transwell membrane with Matrigel and incubating NK cells with or without the presence of a
547 CD44-neutralizing antibody (α-CD44) (**Figure 5A**). We found a statistically significant increase
548 in NK cell invasion in three of four human donor NK cell lines upon α-CD44 treatment (**Figure**
549 **5B**-**E**). To further build on these observations, we employed a 3D *in vitro* model using a tumor
550 spheroid assay (**Figure 5F**). We generated spheroids using the human PDAC PANC-1 cell line
551 and embedded them with human donor NK cells in a Collagen: Matrigel mixture with or without
552 α-CD44 for 24 hours. After incubation, spheroids were stained by immunocytochemistry and
553 imaged. To assess NK cell infiltration, we used pan-cytokeratin staining to outline the spheroids
554 and measured NK cell infiltration into PANC-1 spheroids. Again, under conditions of α-CD44
555 treatment, we observed a statistically significant increase of NK cell invasion using three human
556 donor NK cell lines (**Figure 5G**-**K**, **Supplementary Figure S10**).
557 To explore additional potential mechanisms of action for NK cell invasion, we
558 hypothesized that neutralizing CD44-mediated binding by NK cells would increase the
559 expression of matrix metalloproteinases (MMPs). MMPs are known to degrade ECM, including
560 collagen, can be regulated by CD44, and play a role in neutrophil, macrophage, and T cell

561 migration.[47, 50] Human donor NK cells were treated for 1 and 4 hours with or without α-CD44,
562 and these cells were assessed for expression of MMP genes (**Supplementary Table S5**). We
563 found no significant differences in MMP gene expression across both treatment conditions
564 (**Supplementary Figure S11**), suggesting that antibody-based CD44 neutralization mitigates NK
565 cell binding to ECM components to increase NK cell invasion through matrix-containing
566 environments.

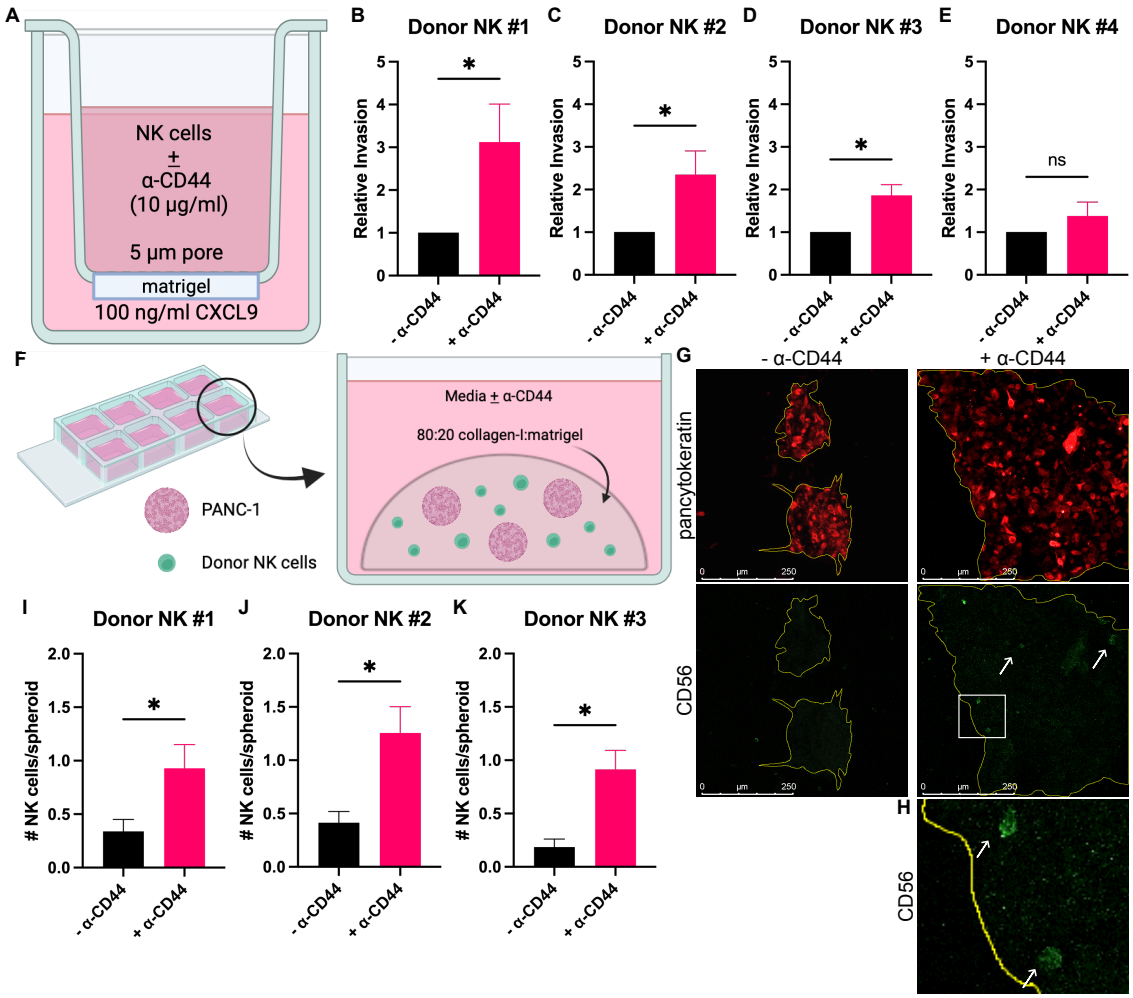

567

568 **Figure 5: CD44 neutralization increases human donor NK cell invasion *in vitro*. A.**
569 Schematic for Transwell invasion assays. Average relative invasion ± SEM of **B.** Donor NK #1
570 (n = 9), **C.** Donor NK #2 (n = 12), **D.** Donor NK #3 (n = 6), and **E.** Donor NK #4 (n = 10) upon

571 CD44 neutralization. *$P < 0.05$ as determined by Wilcoxon matched-pairs signed rank test. **F.**
572 Schematic of spheroid invasion assay. **G.** Representative 20X immunofluorescence images of
573 outlined (yellow) PANC-1 spheroids (pan-cytokeratin; red) embedded with NK cells (CD56;
574 green), pointed out with white arrows, treated with or without α-CD44. Scale bar = 250 µm. **H.**
575 Zoomed inset of NK cells in the α-CD44 treatment group in **G** (white box). Average number of
576 NK cells per PANC-1 spheroid ± SEM from **I.** Donor NK #1 (- α-CD44, n = 42; + α-CD44, n =
577 53), **J.** Donor NK #2 (- α-CD44, n = 43; + α-CD44, n = 29), and **K.** Donor NK #3 (- α-CD44, n =
578 47; + α-CD44, n = 27); n = # of spheroids analyzed; *$P < 0.05$ as determined by Wilcoxon
579 matched-pairs signed rank test.
580

581 **Discussion**

582 While previous studies have used spatial approaches to examine the PDAC TME
583 landscape,[8, 45, 51] NK cells have not been studied extensively. Here, we utilized two single cell
584 methodologies to further characterize NK cells in PDAC. First, we used an IMC spatial
585 proteomics platform to define the spatial relationships of NK cells within the architecture of the
586 human PDAC TME and defined distinct epithelial, fibroblast, and immune cell populations,
587 including NK cells (**Figure 1**). We found for the first time, to our knowledge, that active NK
588 cells are abundant in the PDAC TME and form strong cellular relationships with PDAC
589 epithelial cells. Not only are NK cells relatively abundant and active, but they exist in similar
590 proportions to that of T cell populations across patient samples (**Figure 1-2**), suggesting their
591 potential relevance in PDAC. NK cells were also found within the same cellular neighborhoods
592 that comprise epithelial-ductal regions, and within cellular neighborhood 4, which was immune-
593 rich, thus demonstrating that NK cells localize near epithelial cells, although they are also
594 dispersed across the PDAC TME (**Figure 2C**, **Supplementary Figure S2**). Cellular interaction
595 analysis identified that apoptotic epithelial cells strongly interact with all identified NK cell
596 populations (**Figure 2D**). Distance and network analyses further showed that epithelial cell
597 populations are not only the closest to NK cells, but they also form a strong network with NK
598 cells, indicating they share more neighbors than with other immune cell populations (**Figure 2E-**
599 **F**). Lastly, spatial analyses showed that NK cell localization is inversely proportional to both
600 fibroblast abundance and collagen-I expression in the PDAC TME (**Figure 3**), suggesting that
601 desmoplasia affects NK cell infiltration in PDAC. Therefore, these findings provide novel
602 insights into the spatial relationships of NK cells in untreated human PDAC and highlight

603 potential mechanisms that may limit NK cell invasion in PDAC's malignant epithelial-ductal
604 ROIs.

605 The spatial proteomic analyses were performed in samples from surgically resected
606 primary tumors from previously untreated patients; hence the spatial and functional relationships
607 of NK cells from metastases or primary tumors in a therapeutic setting may differ and remain to
608 be examined. However, our findings provide a benchmark of NK cell function and localization in
609 an untreated setting in primary PDAC tumors. Previous work has primarily assessed or leveraged
610 T cells in monitoring patient prognosis or response to different chemotherapies and
611 immunotherapies.[52] Our findings support the future development of therapies to leverage the
612 biological properties of NK cells in PDAC.

613 Although spatial proteomic analyses provided powerful insights into the NK cellular
614 relationships within the PDAC TME, the IMC antibody panel size was focused to capture
615 representative cell populations across all tissue samples. Accordingly, the IMC panel did not
616 prospectively examine other potentially important proteins that might regulate cell-cell
617 communications. Therefore, to build upon our findings from IMC, we employed a single cell
618 analysis dataset,[33] utilizing CellChat as a secondary tool to further elucidate potential molecular
619 candidates for NK cell interactions in human PDAC. Using CellChat, we found that the *CD44*
620 receptor on NK cells potentially interacts with collagens, laminins, and *FN1* on fibroblasts and
621 malignant epithelial cells (**Figure 4**). As these ligands are known ECM components, and PDAC
622 has a dense, fibrotic stroma, we hypothesized that CD44 on NK cells binds to these molecules,
623 impairing NK cell infiltration towards malignant PDAC cells. Using 2D Transwell and 3D
624 spheroid *in vitro* assays, we made the novel observation that exposure to a CD44-neutralizing
625 antibody significantly increased NK cell invasion (**Figure 5**) through collagen-containing

626 matrices. While CellChat analysis does not provide insights into spatial interactions, as its input
627 requires scRNAseq data, this powerful tool uncovered potential molecular interactions that could
628 be validated *in vitro* and can be investigated further using other methodologies, such as spatial
629 transcriptomics to further uncover potential mechanisms in high versus low fibroblast abundance
630 quartiles in the human PDAC TME.

631 CD44 has been studied in cancer, and its expression is known to be associated with worse
632 prognosis and an increase in metastatic potential in several solid tumors.[47] A recent study
633 showed that liver cancer epithelial cells form cell-in-cell structures of NKp46^{+} NK cells, which
634 has been described to be mediated by loss of CD44 in liver cancer cells.[53] The current IMC
635 dataset identified a NKp44^{+} epithelial cell population. Further studies are needed to determine if
636 these cells contain similar structures to address this phenomenon. CD44 expression in cancers
637 has also been associated with macrophage infiltration and polarization in preclinical models.[54-56]
638 However, there have been limited studies of CD44 in NK cells. CD44 was previously found to
639 be constitutively expressed on IL-2 and IL-15 activated donor NK cells[57, 58] and increased NK
640 cell cytotoxic function.[59] Another study demonstrated that NK cells can elicit redirected lysis
641 through CD44 and CD69 in IL-2 activated NK cells.[57] These studies focused on the role of CD44
642 in NK cell activation, but its role in NK motility has not previously been reported. Interestingly,
643 a study examining the effects of catecholamines in exercise found that NK cells decrease their
644 expression of CD44 and are increased in circulating NK cells in PBMCs, suggesting that CD44
645 plays a role in NK cell adhesion to endothelium and that a decrease in CD44 expression allows
646 for an increase in NK cell extravasation.[60] Therefore, neutralizing NK cell-based CD44 may
647 increase their extravasation, but this has yet to be explored.

648 Here we showed that neutralizing CD44 engagement with ECM components increases
649 NK cell invasion *in vitro*. This is significant because the NK cell-ECM interactome previously
650 has been minimally investigated, even though immune cells are known to express ECM receptors
651 that may affect their motility and immune responses, with implications in solid tumors and
652 fibrotic diseases. One example is LAIR-1, an inhibitory receptor expressed by leukocytes
653 containing collagen-binding domains.[61-63] Another recent study found that fibronectin
654 localization in the center of spheroids composed of small cell renal cell carcinoma cells regulated
655 NK cell infiltration, further supporting a role for ECM components in NK cell migration.[64] These
656 findings, along with data presented here, warrant further investigation, particularly in solid
657 tumors such as PDAC. Hence, targeting selected ECM-NK cell interactions may increase NK
658 cell motility and cytotoxic function for therapeutic benefit. Future studies can determine if CD44
659 plays a role in promoting NK cell-mediated anti-tumor immune responses.

660 **References**

661 1. Siegel, R. L.; Miller, K. D.; Wagle, N. S.; Jemal, A., Cancer statistics, 2023. *CA Cancer*
662 *J Clin* 2023, *73* (1), 17-48.

663 2. Caputo, D., Hot topics in pancreatic cancer management. *World J Gastrointest Surg* 2023,
664 *15* (2), 121-126.

665 3. Karamitopoulou, E., Tumour microenvironment of pancreatic cancer: immune landscape
666 is dictated by molecular and histopathological features. *Br J Cancer* 2019, *121* (1), 5-14.

667 4. Thomas, D.; Radhakrishnan, P., Tumor-stromal crosstalk in pancreatic cancer and tissue
668 fibrosis. *Mol Cancer* 2019, *18* (1), 14.

669 5. Yu, Y.; Yang, G.; Huang, H.; Fu, Z.; Cao, Z.; Zheng, L.; You, L.; Zhang, T., Preclinical
670 models of pancreatic ductal adenocarcinoma: challenges and opportunities in the era of precision
671 medicine. *J Exp Clin Cancer Res* 2021, *40* (1), 8.

672 6. Muller, M.; Haghnejad, V.; Schaefer, M.; Gauchotte, G.; Caron, B.; Peyrin-Biroulet,
673 L.; Bronowicki, J. P.; Neuzillet, C.; Lopez, A., The Immune Landscape of Human Pancreatic
674 Ductal Carcinoma: Key Players, Clinical Implications, and Challenges. *Cancers (Basel)* 2022, *14*
675 (4).

676 7. Ferdek, P. E.; Jakubowska, M. A., Biology of pancreatic stellate cells-more than just
677 pancreatic cancer. *Pflugers Arch* 2017, *469* (9), 1039-1050.

678 8. Liudahl, S. M.; Betts, C. B.; Sivagnanam, S.; Morales-Oyarvide, V.; da Silva, A.; Yuan,
679 C.; Hwang, S.; Grossblatt-Wait, A.; Leis, K. R.; Larson, W.; Lavoie, M. B.; Robinson, P.; Dias
680 Costa, A.; Vayrynen, S. A.; Clancy, T. E.; Rubinson, D. A.; Link, J.; Keith, D.; Horton, W.;
681 Tempero, M. A.; Vonderheide, R. H.; Jaffee, E. M.; Sheppard, B.; Goecks, J.; Sears, R. C.;
682 Park, B. S.; Mori, M.; Nowak, J. A.; Wolpin, B. M.; Coussens, L. M., Leukocyte Heterogeneity

683 in Pancreatic Ductal Adenocarcinoma: Phenotypic and Spatial Features Associated with Clinical
684 Outcome. *Cancer Discov* 2021, *11* (8), 2014-2031.
685 9. Ho, W. J.; Zhu, Q.; Durham, J.; Popovic, A.; Xavier, S.; Leatherman, J.; Mohan, A.;
686 Mo, G.; Zhang, S.; Gross, N.; Charmsaz, S.; Lin, D.; Quong, D.; Wilt, B.; Kamel, I. R.; Weiss,
687 M.; Philosophe, B.; Burkhart, R.; Burns, W. R.; Shubert, C.; Ejaz, A.; He, J.; Deshpande, A.;
688 Danilova, L.; Stein-O'Brien, G.; Sugar, E. A.; Laheru, D. A.; Anders, R. A.; Fertig, E. J.; Jaffee,
689 E. M.; Yarchoan, M., Neoadjuvant cabozantinib and nivolumab convert locally advanced
690 hepatocellular carcinoma into resectable disease with enhanced antitumor immunity. *Nature*
691 *Cancer* 2021, *2* (9), 891-903.
692 10. Le Rochais, M.; Hemon, P.; Pers, J. O.; Uguen, A., Application of High-Throughput
693 Imaging Mass Cytometry Hyperion in Cancer Research. *Front Immunol* 2022, *13*, 859414.
694 11. Ali, H. R.; Jackson, H. W.; Zanotelli, V. R. T.; Danenberg, E.; Fischer, J. R.; Bardwell,
695 H.; Provenzano, E.; Team, C. I. G. C.; Rueda, O. M.; Chin, S. F.; Aparicio, S.; Caldas, C.;
696 Bodenmiller, B., Imaging mass cytometry and multiplatform genomics define the phenogenomic
697 landscape of breast cancer. *Nat Cancer* 2020, *1* (2), 163-175.
698 12. Chang, Q.; Ornatsky, O. I.; Siddiqui, I.; Straus, R.; Baranov, V. I.; Hedley, D. W.,
699 Biodistribution of cisplatin revealed by imaging mass cytometry identifies extensive collagen
700 binding in tumor and normal tissues. *Sci Rep* 2016, *6*, 36641.
701 13. Kuett, L.; Catena, R.; Ozcan, A.; Pluss, A.; Cancer Grand Challenges, I. C.; Schraml,
702 P.; Moch, H.; de Souza, N.; Bodenmiller, B., Three-dimensional imaging mass cytometry for
703 highly multiplexed molecular and cellular mapping of tissues and the tumor microenvironment.
704 *Nat Cancer* 2022, *3* (1), 122-133.

705 14. Sheng, J.; Zhang, J.; Wang, L.; Tano, V.; Tang, J.; Wang, X.; Wu, J.; Song, J.; Zhao,
706 Y.; Rong, J.; Cheng, F.; Wang, J.; Shen, Y.; Wen, L.; He, J.; Zhang, H.; Li, T.; Zhang, Q.;
707 Bai, X.; Lu, Z.; Liang, T., Topological analysis of hepatocellular carcinoma tumour
708 microenvironment based on imaging mass cytometry reveals cellular neighbourhood regulated
709 reversely by macrophages with different ontogeny. *Gut* 2022, *71* (6), 1176-1191.
710 15. Fitzgerald, A. A.; Wang, S.; Agarwal, V.; Marcisak, E. F.; Zuo, A.; Jablonski, S. A.;
711 Loth, M.; Fertig, E. J.; MacDougall, J.; Zhukovsky, E.; Trivedi, S.; Bhatia, D.; O'Neill, V.;
712 Weiner, L. M., DPP inhibition alters the CXCR3 axis and enhances NK and CD8+ T cell
713 infiltration to improve anti-PD1 efficacy in murine models of pancreatic ductal adenocarcinoma.
714 *J Immunother Cancer* 2021, *9* (11).
715 16. Jewett, A.; Kos, J.; Kaur, K.; Safaei, T.; Sutanto, C.; Chen, W.; Wong, P.; Namagerdi,
716 A. K.; Fang, C.; Fong, Y.; Ko, M. W., Natural Killer Cells: Diverse Functions in Tumor Immunity
717 and Defects in Pre-neoplastic and Neoplastic Stages of Tumorigenesis. *Mol Ther Oncolytics* 2020,
718 *16*, 41-52.
719 17. Malchiodi, Z. X.; Weiner, L. M., Understanding and Targeting Natural Killer Cell-Cancer-
720 Associated Fibroblast Interactions in Pancreatic Ductal Adenocarcinoma. *Cancers (Basel)* 2021,
721 *13* (3).
722 18. Van Audenaerde, J. R. M.; Roeyen, G.; Darcy, P. K.; Kershaw, M. H.; Peeters, M.;
723 Smits, E. L. J., Natural killer cells and their therapeutic role in pancreatic cancer: A systematic
724 review. *Pharmacol Ther* 2018, *189*, 31-44.
725 19. Chang, Q.; Ornatsky, O. I.; Siddiqui, I.; Loboda, A.; Baranov, V. I.; Hedley, D. W.,
726 Imaging Mass Cytometry. *Cytometry A* 2017, *91* (2), 160-169.

727 20. Delgado-Gonzalez, A.; Sanchez-Martin, R. M., Mass Cytometry Tags: Where Chemistry
728 Meets Single-Cell Analysis. *Anal Chem* 2021, *93* (2), 657-664.
729 21. Wang, Y. J.; Traum, D.; Schug, J.; Gao, L.; Liu, C.; Consortium, H.; Atkinson, M. A.;
730 Powers, A. C.; Feldman, M. D.; Naji, A.; Chang, K. M.; Kaestner, K. H., Multiplexed In Situ
731 Imaging Mass Cytometry Analysis of the Human Endocrine Pancreas and Immune System in Type
732 1 Diabetes. *Cell Metab* 2019, *29* (3), 769-783 e4.
733 22. Jackson, H. W.; Fischer, J. R.; Zanotelli, V. R. T.; Ali, H. R.; Mechera, R.; Soysal, S.
734 D.; Moch, H.; Muenst, S.; Varga, Z.; Weber, W. P.; Bodenmiller, B., The single-cell pathology
735 landscape of breast cancer. *Nature* 2020, *578* (7796), 615-620.
736 23. Hoch, T.; Schulz, D.; Eling, N.; Gomez, J. M.; Levesque, M. P.; Bodenmiller, B.,
737 Multiplexed imaging mass cytometry of the chemokine milieus in melanoma characterizes features
738 of the response to immunotherapy. *Sci Immunol* 2022, *7* (70), eabk1692.
739 24. Windhager, J.; Zanotelli, V. R. T.; Schulz, D.; Meyer, L.; Daniel, M.; Bodenmiller, B.;
740 Eling, N., An end-to-end workflow for multiplexed image processing and analysis. *Nat Protoc*
741 2023, *18* (11), 3565-3613.
742 25. Berg, S.; Kutra, D.; Kroeger, T.; Straehle, C. N.; Kausler, B. X.; Haubold, C.; Schiegg,
743 M.; Ales, J.; Beier, T.; Rudy, M.; Eren, K.; Cervantes, J. I.; Xu, B.; Beuttenmueller, F.; Wolny,
744 A.; Zhang, C.; Koethe, U.; Hamprecht, F. A.; Kreshuk, A., ilastik: interactive machine learning
745 for (bio)image analysis. *Nat Methods* 2019, *16* (12), 1226-1232.
746 26. Schapiro, D.; Jackson, H. W.; Raghuraman, S.; Fischer, J. R.; Zanotelli, V. R. T.; Schulz,
747 D.; Giesen, C.; Catena, R.; Varga, Z.; Bodenmiller, B., histoCAT: analysis of cell phenotypes
748 and interactions in multiplex image cytometry data. *Nat Methods* 2017, *14* (9), 873-876.

749 27. Hao, Y.; Hao, S.; Andersen-Nissen, E.; Mauck, W. M., 3rd; Zheng, S.; Butler, A.; Lee,
750 M. J.; Wilk, A. J.; Darby, C.; Zager, M.; Hoffman, P.; Stoeckius, M.; Papalexi, E.; Mimitou,
751 E. P.; Jain, J.; Srivastava, A.; Stuart, T.; Fleming, L. M.; Yeung, B.; Rogers, A. J.; McElrath,
752 J. M.; Blish, C. A.; Gottardo, R.; Smibert, P.; Satija, R., Integrated analysis of multimodal single-
753 cell data. *Cell* 2021, *184* (13), 3573-3587 e29.
754 28. Amezquita, R. A.; Lun, A. T. L.; Becht, E.; Carey, V. J.; Carpp, L. N.; Geistlinger, L.;
755 Marini, F.; Rue-Albrecht, K.; Risso, D.; Soneson, C.; Waldron, L.; Pages, H.; Smith, M. L.;
756 Huber, W.; Morgan, M.; Gottardo, R.; Hicks, S. C., Orchestrating single-cell analysis with
757 Bioconductor. *Nat Methods* 2020, *17* (2), 137-145.
758 29. Righelli, D.; Weber, L. M.; Crowell, H. L.; Pardo, B.; Collado-Torres, L.; Ghazanfar,
759 S.; Lun, A. T. L.; Hicks, S. C.; Risso, D., SpatialExperiment: infrastructure for spatially-resolved
760 transcriptomics data in R using Bioconductor. *Bioinformatics* 2022, *38* (11), 3128-3131.
761 30. Goltsev, Y.; Samusik, N.; Kennedy-Darling, J.; Bhate, S.; Hale, M.; Vazquez, G.; Black,
762 S.; Nolan, G. P., Deep Profiling of Mouse Splenic Architecture with CODEX Multiplexed
763 Imaging. *Cell* 2018, *174* (4), 968-981 e15.
764 31. Schurch, C. M.; Bhate, S. S.; Barlow, G. L.; Phillips, D. J.; Noti, L.; Zlobec, I.; Chu,
765 P.; Black, S.; Demeter, J.; McIlwain, D. R.; Kinoshita, S.; Samusik, N.; Goltsev, Y.; Nolan, G.
766 P., Coordinated Cellular Neighborhoods Orchestrate Antitumoral Immunity at the Colorectal
767 Cancer Invasive Front. *Cell* 2020, *182* (5), 1341-1359 e19.
768 32. Lee, C. W.; Ren, Y. J.; Marella, M.; Wang, M.; Hartke, J.; Couto, S. S., Multiplex
769 immunofluorescence staining and image analysis assay for diffuse large B cell lymphoma. *J*
770 *Immunol Methods* 2020, *478*, 112714.

771 33. Steele, N. G.; Carpenter, E. S.; Kemp, S. B.; Sirihorachai, V. R.; The, S.; Delrosario,
772 L.; Lazarus, J.; Amir, E. D.; Gunchick, V.; Espinoza, C.; Bell, S.; Harris, L.; Lima, F.; Irizarry-
773 Negron, V.; Paglia, D.; Macchia, J.; Chu, A. K. Y.; Schofield, H.; Wamsteker, E. J.; Kwon,
774 R.; Schulman, A.; Prabhu, A.; Law, R.; Sondhi, A.; Yu, J.; Patel, A.; Donahue, K.; Nathan,
775 H.; Cho, C.; Anderson, M. A.; Sahai, V.; Lyssiotis, C. A.; Zou, W.; Allen, B. L.; Rao, A.;
776 Crawford, H. C.; Bednar, F.; Frankel, T. L.; Pasca di Magliano, M., Multimodal Mapping of the
777 Tumor and Peripheral Blood Immune Landscape in Human Pancreatic Cancer. *Nat Cancer* 2020,
778 *1* (11), 1097-1112.
779 34. Gulati, G. S.; Sikandar, S. S.; Wesche, D. J.; Manjunath, A.; Bharadwaj, A.; Berger, M.
780 J.; Ilagan, F.; Kuo, A. H.; Hsieh, R. W.; Cai, S.; Zabala, M.; Scheeren, F. A.; Lobo, N. A.;
781 Qian, D.; Yu, F. B.; Dirbas, F. M.; Clarke, M. F.; Newman, A. M., Single-cell transcriptional
782 diversity is a hallmark of developmental potential. *Science* 2020, *367* (6476), 405-411.
783 35. Scrucca, L.; Fop, M.; Murphy, T. B.; Raftery, A. E., mclust 5: Clustering, Classification
784 and Density Estimation Using Gaussian Finite Mixture Models. *R J* 2016, *8* (1), 289-317.
785 36. Jin, S.; Guerrero-Juarez, C. F.; Zhang, L.; Chang, I.; Ramos, R.; Kuan, C. H.; Myung,
786 P.; Plikus, M. V.; Nie, Q., Inference and analysis of cell-cell communication using CellChat. *Nat*
787 *Commun* 2021, *12* (1), 1088.
788 37. Aldeghaither, D. S.; Zahavi, D. J.; Murray, J. C.; Fertig, E. J.; Graham, G. T.; Zhang,
789 Y. W.; O'Connell, A.; Ma, J.; Jablonski, S. A.; Weiner, L. M., A Mechanism of Resistance to
790 Antibody-Targeted Immune Attack. *Cancer Immunol Res* 2019, *7* (2), 230-243.
791 38. Carr, W. H.; Zinsou, C.; Rowe, T.; Lange, C.; Lawal, O. O., Human natural killer cell
792 expansion in vitro using mitomycin-C treatment as an alternative to irradiation of modified K562
793 feeder cells. *The Journal of Immunology* 2017, *198* (1_Supplement), 82.16-82.16.

794 39. Schindelin, J.; Arganda-Carreras, I.; Frise, E.; Kaynig, V.; Longair, M.; Pietzsch, T.;
795 Preibisch, S.; Rueden, C.; Saalfeld, S.; Schmid, B.; Tinevez, J. Y.; White, D. J.; Hartenstein,
796 V.; Eliceiri, K.; Tomancak, P.; Cardona, A., Fiji: an open-source platform for biological-image
797 analysis. *Nat Methods* 2012, *9* (7), 676-82.
798 40. Lin, Y. N.; Nasir, A.; Camacho, S.; Berry, D. L.; Schmidt, M. O.; Pearson, G. W.;
799 Riegel, A. T.; Wellstein, A., Monitoring Cancer Cell Invasion and T-Cell Cytotoxicity in 3D
800 Culture. *J Vis Exp* 2020, (160).
801 41. Iyer, A.; Hamers, A. A. J.; Pillai, A. B., CyTOF((R)) for the Masses. *Front Immunol* 2022,
802 *13*, 815828.
803 42. Giesen, C.; Wang, H. A.; Schapiro, D.; Zivanovic, N.; Jacobs, A.; Hattendorf, B.;
804 Schuffler, P. J.; Grolimund, D.; Buhmann, J. M.; Brandt, S.; Varga, Z.; Wild, P. J.; Gunther,
805 D.; Bodenmiller, B., Highly multiplexed imaging of tumor tissues with subcellular resolution by
806 mass cytometry. *Nat Methods* 2014, *11* (4), 417-22.
807 43. Hafemeister, C.; Satija, R., Normalization and variance stabilization of single-cell RNA-
808 seq data using regularized negative binomial regression. *Genome Biol* 2019, *20* (1), 296.
809 44. Mi, H.; Ho, W. J.; Yarchoan, M.; Popel, A. S., Multi-Scale Spatial Analysis of the Tumor
810 Microenvironment Reveals Features of Cabozantinib and Nivolumab Efficacy in Hepatocellular
811 Carcinoma. *Front Immunol* 2022, *13*, 892250.
812 45. Carstens, J. L.; Correa de Sampaio, P.; Yang, D.; Barua, S.; Wang, H.; Rao, A.; Allison,
813 J. P.; LeBleu, V. S.; Kalluri, R., Spatial computation of intratumoral T cells correlates with
814 survival of patients with pancreatic cancer. *Nature Communications* 2017, *8* (1), 15095.

815 46. Enane, F. O.; Saunthararajah, Y.; Korc, M., Differentiation therapy and the mechanisms
816 that terminate cancer cell proliferation without harming normal cells. *Cell Death Dis* 2018, *9* (9),
817 912.
818 47. Chen, C.; Zhao, S.; Karnad, A.; Freeman, J. W., The biology and role of CD44 in cancer
819 progression: therapeutic implications. *J Hematol Oncol* 2018, *11* (1), 64.
820 48. Weng, X.; Maxwell-Warburton, S.; Hasib, A.; Ma, L.; Kang, L., The membrane receptor
821 CD44: novel insights into metabolism. *Trends Endocrinol Metab* 2022, *33* (5), 318-332.
822 49. Guo, Q.; Yang, C.; Gao, F., The state of CD44 activation in cancer progression and
823 therapeutic targeting. *FEBS J* 2022, *289* (24), 7970-7986.
824 50. McMahon, M.; Ye, S.; Pedrina, J.; Dlugolenski, D.; Stambas, J., Extracellular Matrix
825 Enzymes and Immune Cell Biology. *Front Mol Biosci* 2021, *8*, 703868.
826 51. Hwang, W. L.; Jagadeesh, K. A.; Guo, J. A.; Hoffman, H. I.; Yadollahpour, P.; Reeves,
827 J. W.; Mohan, R.; Drokhlyansky, E.; Van Wittenberghe, N.; Ashenberg, O.; Farhi, S. L.;
828 Schapiro, D.; Divakar, P.; Miller, E.; Zollinger, D. R.; Eng, G.; Schenkel, J. M.; Su, J.; Shiau,
829 C.; Yu, P.; Freed-Pastor, W. A.; Abbondanza, D.; Mehta, A.; Gould, J.; Lambden, C.; Porter,
830 C. B. M.; Tsankov, A.; Dionne, D.; Waldman, J.; Cuoco, M. S.; Nguyen, L.; Delorey, T.;
831 Phillips, D.; Barth, J. L.; Kem, M.; Rodrigues, C.; Ciprani, D.; Roldan, J.; Zelga, P.; Jorgji,
832 V.; Chen, J. H.; Ely, Z.; Zhao, D.; Fuhrman, K.; Fropf, R.; Beechem, J. M.; Loeffler, J. S.;
833 Ryan, D. P.; Weekes, C. D.; Ferrone, C. R.; Qadan, M.; Aryee, M. J.; Jain, R. K.; Neuberg, D.
834 S.; Wo, J. Y.; Hong, T. S.; Xavier, R.; Aguirre, A. J.; Rozenblatt-Rosen, O.; Mino-Kenudson,
835 M.; Castillo, C. F.; Liss, A. S.; Ting, D. T.; Jacks, T.; Regev, A., Single-nucleus and spatial
836 transcriptome profiling of pancreatic cancer identifies multicellular dynamics associated with
837 neoadjuvant treatment. *Nat Genet* 2022, *54* (8), 1178-1191.

838 52. Hester, R.; Mazur, P. K.; McAllister, F., Immunotherapy in Pancreatic Adenocarcinoma:
839 Beyond "Copy/Paste". *Clin Cancer Res* 2021, *27* (23), 6287-6297.
840 53. Su, Y.; Huang, H.; Luo, T.; Zheng, Y.; Fan, J.; Ren, H.; Tang, M.; Niu, Z.; Wang, C.;
841 Wang, Y.; Zhang, Z.; Liang, J.; Ruan, B.; Gao, L.; Chen, Z.; Melino, G.; Wang, X.; Sun, Q.,
842 Cell-in-cell structure mediates in-cell killing suppressed by CD44. *Cell Discov* 2022, *8* (1), 35.
843 54. Liu, S.; Liu, Z.; Shang, A.; Xun, J.; Lv, Z.; Zhou, S.; Liu, C.; Zhang, Q.; Yang, Y.,
844 CD44 is a potential immunotherapeutic target and affects macrophage infiltration leading to poor
845 prognosis. *Sci Rep* 2023, *13* (1), 9657.
846 55. Rios de la Rosa, J. M.; Tirella, A.; Gennari, A.; Stratford, I. J.; Tirelli, N., The CD44-
847 Mediated Uptake of Hyaluronic Acid-Based Carriers in Macrophages. *Adv Healthc Mater* 2017,
848 *6* (4).
849 56. Vey, N.; Delaunay, J.; Martinelli, G.; Fiedler, W.; Raffoux, E.; Prebet, T.; Gomez-
850 Roca, C.; Papayannidis, C.; Kebenko, M.; Paschka, P.; Christen, R.; Guarin, E.; Broske, A.
851 M.; Baehner, M.; Brewster, M.; Walz, A. C.; Michielin, F.; Runza, V.; Meresse, V.; Recher,
852 C., Phase I clinical study of RG7356, an anti-CD44 humanized antibody, in patients with acute
853 myeloid leukemia. *Oncotarget* 2016, *7* (22), 32532-42.
854 57. Sconocchia, G.; Titus, J. A.; Segal, D. M., Signaling Pathways Regulating CD44-
855 Dependent Cytolysis in Natural Killer Cells. *Blood* 1997, *90* (2), 716-725.
856 58. Paul, S.; Lal, G., The Molecular Mechanism of Natural Killer Cells Function and Its
857 Importance in Cancer Immunotherapy. *Front Immunol* 2017, *8*, 1124.
858 59. Sague, S. L.; Tato, C.; Pure, E.; Hunter, C. A., The regulation and activation of CD44 by
859 natural killer (NK) cells and its role in the production of IFN-gamma. *J Interferon Cytokine Res*
860 2004, *24* (5), 301-9.

861 60. Nagao, F.; Suzui, M.; Takeda, K.; Yagita, H.; Okumura, K., Mobilization of NK cells by
862 exercise: downmodulation of adhesion molecules on NK cells by catecholamines. *Am J Physiol*
863 *Regul Integr Comp Physiol* 2000, *279* (4), R1251-6.
864 61. Vyas, M.; Peigney, D.; Demehri, S., Extracellular matrix-natural killer cell interactome:
865 an uncharted territory in health and disease. *Curr Opin Immunol* 2022, *78*, 102246.
866 62. Vyas, M.; Demehri, S., The extracellular matrix and immunity: breaking the old barrier in
867 cancer. *Trends Immunol* 2022, *43* (6), 423-425.
868 63. Carvalheiro, T.; Garcia, S.; Pascoal Ramos, M. I.; Giovannone, B.; Radstake, T.; Marut,
869 W.; Meyaard, L., Leukocyte Associated Immunoglobulin Like Receptor 1 Regulation and
870 Function on Monocytes and Dendritic Cells During Inflammation. *Front Immunol* 2020, *11*, 1793.
871 64. Rajasekaran, N.; House, T.; Magdaleno, C. C.; Varadaraj, A., Assembly and localization
872 of extracellular matrix protein fibronectin modulates Natural killer cell infiltration in tumor
873 spheroids. *The Journal of Immunology* 2022, *208* (1_Supplement), 62.08-62.08.
874